Temperature dependence of nanostructure in PbSe–ZnSe composite thin film

Yojiro Oba,[1] Seishi Abe,[2] Masato Ohnuma,[3] Nobuhiro Sato[1] and Masaaki Sugiyama[1]

[1]Kyoto University Research Reactor Institute, Kumatori, Osaka 590-0494, Japan

[2]Research Institute for Electromagnetic Materials, Sendai, Miyagi 982-0807, Japan

[3]Hokkaido University, Sapporo, Hokkaido 060-8628, Japan

Abstract

The nanostructure of PbSe–ZnSe composite thin films prepared by the hot-wall deposition (HWD) method was investigated using small-angle x-ray (SAXS) scattering. The SAXS profiles indicate the formation of two kinds of nanoparticles: large nanoparticles that vanish and small particles that increase in size with increasing temperature. At high substrate temperatures, the volume fraction of all the nanoparticles estimated from SAXS is consistent with that of PbSe obtained by chemical analysis. This shows that PbSe forms nanoparticles at high substrate temperatures. On the other hand, the same analysis for the volume fraction at low substrate temperatures reveals that the chemical composition of the nanoparticles differs from PbSe. Pb nanoparticles are probably formed at low substrate temperatures and disappear with increasing substrate temperature.

1. Introduction

Quantum-dot solar cells are now one of the most important materials available for reducing the use of fossil fuels and environmental pollution. Since its optical band gap can be tuned by controlling the quantum size effects, high conversion efficiencies optimized for the solar spectrum are achievable [1,2]. Furthermore, the quantum size effects can provide higher photovoltages through collection of hot carriers

or higher photocurrents through an enhanced impact ionization process. Indeed, it was predicted that the ideal thermodynamic conversion efficiency of the quantum-dot solar cells could reach up to 66% [2]. Experimentally, a peak external quantum efficiency of 114% was reported [3].

PbSe, which makes control of the quantum size effect easy, is a promising material for quantum-dot sensitizers because of a large exciton Bohr radius of 46 nm [4,5]. The PbSe–ZnSe system in particular is an attractive composite for quantum-dot solar cells [6–8]. Both PbSe and ZnSe are well-known semiconductors with band gaps of 0.27 and 2.7 eV in the bulk state, respectively. This large difference in the band gaps is suitable for utilization of the full solar spectrum [6]. Recently, one-step synthesis of a PbSe–ZnSe composite thin film using hot-wall deposition (HWD) was developed [7]. In this preparation method, both PbSe and ZnSe are simultaneously evaporated from separate sources through a heated wall. Since the deposition process of HWD is close to thermal equilibrium conditions between deposition and re-evaporation on the substrate and the PbSe-ZnSe system has a very low solubility limit, PbSe quantum dots were clearly separated from the ZnSe matrix on the substrate. This enables easy preparation of high-quality composite thin films. Although there are a lot of reports about PbSe quantum dots synthesised by wet chemical methods [5, 6], HWD has an advantage that it can make the composite thin films in *one step*. This is effective for low-cost mass production. In contrast, the advantage of the wet chemical synthesis methods is production of highly monodispersed quantum dots. However, the monodispersity is achieved by centrifuge separation process of by-products, unreacted precursors, and aggregated nanoparticles following the formation of the quantum dots. To make the composite thin films, a film-forming process of quantum dots such as spin coating is also needed [6].

To control the quantum size effects and produce optimal photovoltaic properties, precise characterization of the morphology of the quantum dot is required. In a previous study, the quantum effects were not elucidated owing to the lack of structural information [7]. Therefore, we conducted a small-angle x-ray scattering (SAXS) analysis in order to investigate the nanostructure of the PbSe–ZnSe composite thin film. Although information obtained from SAXS is not straightforward because of reciprocal space analysis, SAXS has a great advantage in terms of observable volume and statistical

accuracy as compared with conventional techniques such as transmission electron microscopy (TEM) and so on [9,10]. Hence, SAXS is a suitable method (or technique) for analyzing the size distribution of the nanoparticles and the fractional change. These characteristics are useful for investigating the growth process and improving the preparation conditions of the nanoparticles. There are not a few reports about the *qualitative* characterization of nanoparticles such as quantum dots in composite thin films using SAXS [9,11–13]. Therefore, in this study, the nanostructure of the PbSe–ZnSe composite thin films was quantitatively investigated using SAXS.

2. Experimental procedure

PbSe–ZnSe composite thin films were prepared by HWD, which is a vacuum evaporation method under an atmosphere near thermal equilibrium between the deposition to the substrate and re-evaporation from the substrate. The parameters affecting the formation of the nanostructure are the temperatures of the PbSe and ZnSe sources, the wall, and the substrate. Details of the preparation were reported in a previous paper [7]. To change the size of the PbSe quantum dot, the temperature of the substrate, T_{sub}, was changed in the present experiment. For this purpose, the temperature of the cooling water for the substrate, T_{water}, and the temperature of the wall, T_{wall}, were controlled (table 1). The values of T_{sub} were checked by a temperature indicator (THERMOLABEL™, NiGK Corp.) placed near the substrate and the values are listed in table 1. However, T_{sub} of samples 4 and 5 exceeded the range of the temperature indicator. Hence, only the relative order of T_{sub} was inferred for these samples from T_{water} and T_{wall}. Since T_{wall} of sample 4 was the same as that of sample 3 and T_{water} was higher than that of sample 3, T_{sub} of sample 4 must be higher than that of sample 3. Similarly, T_{sub} of sample 5 was thought to be higher than that of sample 4. To suppress background scattering from the substrate, which would interfere with the SAXS measurements, the films were deposited on single-crystal Si substrates with a thickness of 0.5 mm. The chemical composition of x in $(PbSe)_x(ZnSe)_{1-x}$ was determined using energy dispersive x-ray spectroscopy (EDX) and is also listed in table 1.

SAXS measurements were performed using a SAXS instrument (Nano-viewer, RIGAKU), which is a conventional transmission-type optical system. To measure the thin films through the substrates, Mo Kα radiation (0.071 nm), which has higher penetration power than conventional Cu Kα radiation, was used. The incident x-ray was focused using a two-dimensional confocal mirror and was collimated using the pinhole technique. The scattered x-ray was detected with a two-dimensional detector (PILATUS 100k). The beam diameter at the sample was ~0.5 mm. The SAXS was measured with two distances between the samples and the detector, 0.35 and 1.4 m, respectively, which covers a q range from 0.1 to 11 nm^{-1}. Here, q ($=4\pi\sin\theta/\lambda$) is a momentum transfer. The parameters θ and λ are half of the scattering angle and the wavelength of the incident x-ray, respectively. In order to obtain the SAXS profile only from the thin film, the profiles of the Si substrates were measured and subtracted from the SAXS profiles of the samples. A glassy carbon characterized at the Argonne National Laboratory was used as a standard to convert the scattering intensity in absolute units [14].

Table 1. T_{water}, T_{wall}, T_{sub}, and mole fraction x of the $(PbSe)_x(ZnSe)_{1-x}$ composite thin films. $D_{Scherrer}$ is also listed.

Sample	T_{water} (°C)	T_{wall} (°C)	T_{sub} (°C)	x	$D_{Scherrer}$ (nm)
1	1	783	130		
2	77	723	150	0.17	8
3	55	783	210	0.16	9
4	60	783	>220	0.12	10
5	77	783	>220	0.13	10

3. Results and Discussion

Figure 1 shows the SAXS profiles of all the samples. Scattering was clearly observed between q = 0.2 and 3 nm^{-1}. All the profiles show a plateau at the lowest q (roughly $q < 0.5$ nm^{-1}), and the profiles at the

higher q range decreased in proportion to q^{-4}. Similar behaviour is observed in the scattering of spherical particles, confirming the formation of nanoparticles in the samples [12,13]. The interesting point is that with increasing T_{sub}, a peculiar change the SAXS profile occurs. From sample 1 to sample 2, a broad peak appears at $q \approx 0.5$ nm^{-1}. This peak indicates the interparticle interference effect, which means that the nanoparticles are densely packed in the thin films [15,16]. Since the intensity of the profile increases, either the volume fraction of the nanoparticles or the scattering contrast $\Delta\rho^2$ increases, as will be discussed in a later section. Contrary to the change between samples 1 and 2, the intensity of sample 3 decreases. The decrease indicates a decrease either in the volume fraction of the nanoparticles or the scattering contrast. Between samples 2 and 3, the curvature of the profile increases. This suggests that the size distribution decreases. The SAXS profiles of samples 3, 4, and 5 systematically change. The plateau at $q \approx 0.4$ nm^{-1} (indicated by dotted line in figure 1) shifts to a lower q and a higher intensity, and the peak of the interparticle interference becomes weak. These characteristics indicate the coarsening of the nanoparticles. Except for the decrease in intensity observed in sample 3, these qualitative features of temperature dependence indicate that the nanoparticles grow and coarsen with increasing temperature.

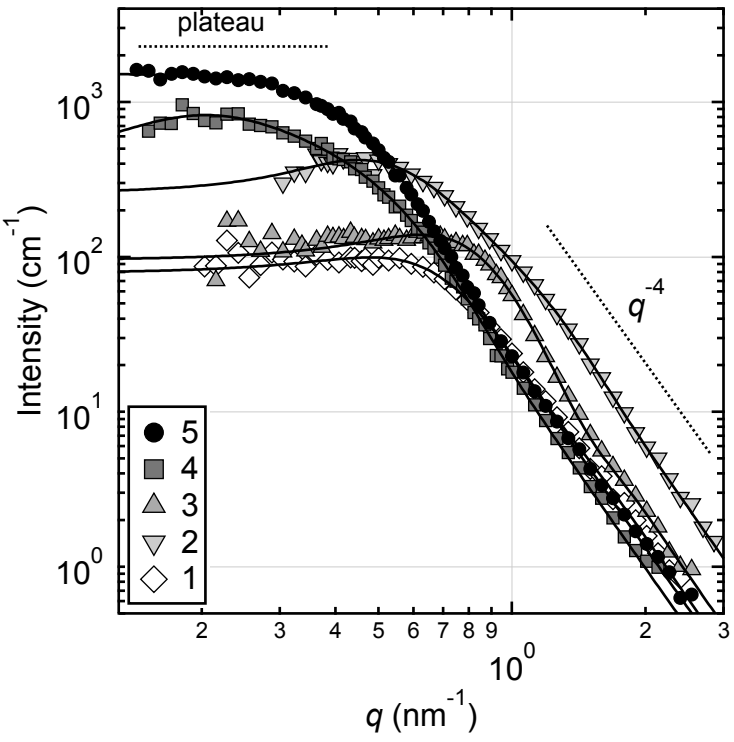

Figure 1. SAXS profiles of the PbSe–ZnSe composite thin films. Markers and solid lines are experimental data and fitted curve, respectively. Dotted lines are visual guides for the plateau and q^{-4} behaviours.

For detailed analysis, curve fitting was carried out using structural models. A particle system exhibiting the interparticle interference effect was chosen as the fitting model. The local monodisperse approximation was used to incorporate the size distribution into the interparticle interference effect [16]. This approximation assumes that the particles are locally monodispersed. The fit function is written as

$$I(q) = d_N \Delta\rho^2 \int_0^\infty V^2 N(r) F^2(q,r) S(q,r)\, dr\,, \qquad (1)$$

or

$$I(q) = d_N \Delta\rho^2 \int_0^\infty V N_V(r) F^2(q,r) S(q,r)\, dr\,, \qquad (2)$$

where d_N is the number density of particles. Both d_N and $\Delta\rho^2$ are independent of q and r. The parameters r and V are the radius and volume of the particles, respectively. $F(q,r)$ is the form factor, which is determined from the particle shape, and $S(q,r)$ is the structure factor, which represents the interparticle interference effect. The functions $N(r)$ and $N_V(r)$ are the number and volume fraction size distributions, respectively, where $N_V(r) = VN(r)$ [17,18]. In the present samples, $N_V(r)$ is a good indicator of the representative size because photoabsorption properties are governed by the volume fraction rather than by the number of particles. The function $F(q)$ was considered based on our previous study [7]. In this study, the TEM image of the PbSe-ZnSe clearly showed that the formation of nanoparticles. Although there were various shapes of nanoparticles, isotropic nanoparticles were dominant. In such case, a spherical shape is a good approximation as the shape of the nanoparticles. The characteristics of the SAXS profiles,

i.e. a plateau immediately followed by q^{-4}, also confirm the spherical shape [15]. Since no q^{-a} (a<4) behaviour is observed, the possibility of anisotropic shapes such as rod, disc, and ellipsoid of revolution is denied. For the spherical nanoparticles, $F(q)$ and V are given by [15]

$$F(q,r) = 3\frac{\sin(qr) - qr\cos(qr)}{(qr)^3}, \qquad (3)$$

$$V = \frac{4}{3}\pi r^3. \qquad (4)$$

For $N(r)$, the previous TEM observation provided almost no information due to very small number of the observed nanoparticles. Therefore, a Gaussian distribution function was chosen as a first approximation. Although a logarithmic distribution function was also tested, the Gaussian function gave better results. For accurate comparison of the results, $N(r)$ was fixed as the Gaussian throughout the present samples. Therefore, $N(r)$ is represented as

$$N(r) = \frac{1}{\sqrt{2\pi}\sigma}\exp\left\{-\frac{\left(r - r_{ave}\right)^2}{2\sigma^2}\right\}, \qquad (5)$$

where r_{ave} and σ are the average and standard deviation of the radius, respectively. However, for samples 1 and 2, neither a simple Gaussian function nor a logarithmic normal function could explain the SAXS profiles. As the result of trials with several functions, we found that a set of two Gaussian functions with the different r_{ave} and σ, $N_{total}(r) = N_S(r) + N_L(r)$ produced the best fit, where $N_{total}(r)$ is normalized as

$$\int_0^\infty N_{total}(r)\,dr = 1. \qquad (6)$$

$N_S(r)$ and $N_L(r)$ represent Gaussian functions with peak positions at smaller and larger diameters, respectively. Although a combination of three Gaussian functions slightly improved the shape of the fit curve, the accuracy of the obtained parameters was degraded as a result of too many parameters. The Percus–Yevick approximation with a hard-sphere potential was selected for $S(q)$ [15]. The Percus–Yevick model is interpreted by two parameters: the volume fraction of the particles, V_{hs}, and the interaction radius, r_{hs}. Figure 1 also shows the fitting results. They well reproduced the experimental results. Note that the set of two Gaussian functions was just an empirical choice based on the SAXS profiles; they had no physical meaning at this point. Nevertheless, the result of the fitting infers that the samples probably consist of two kinds of particles.

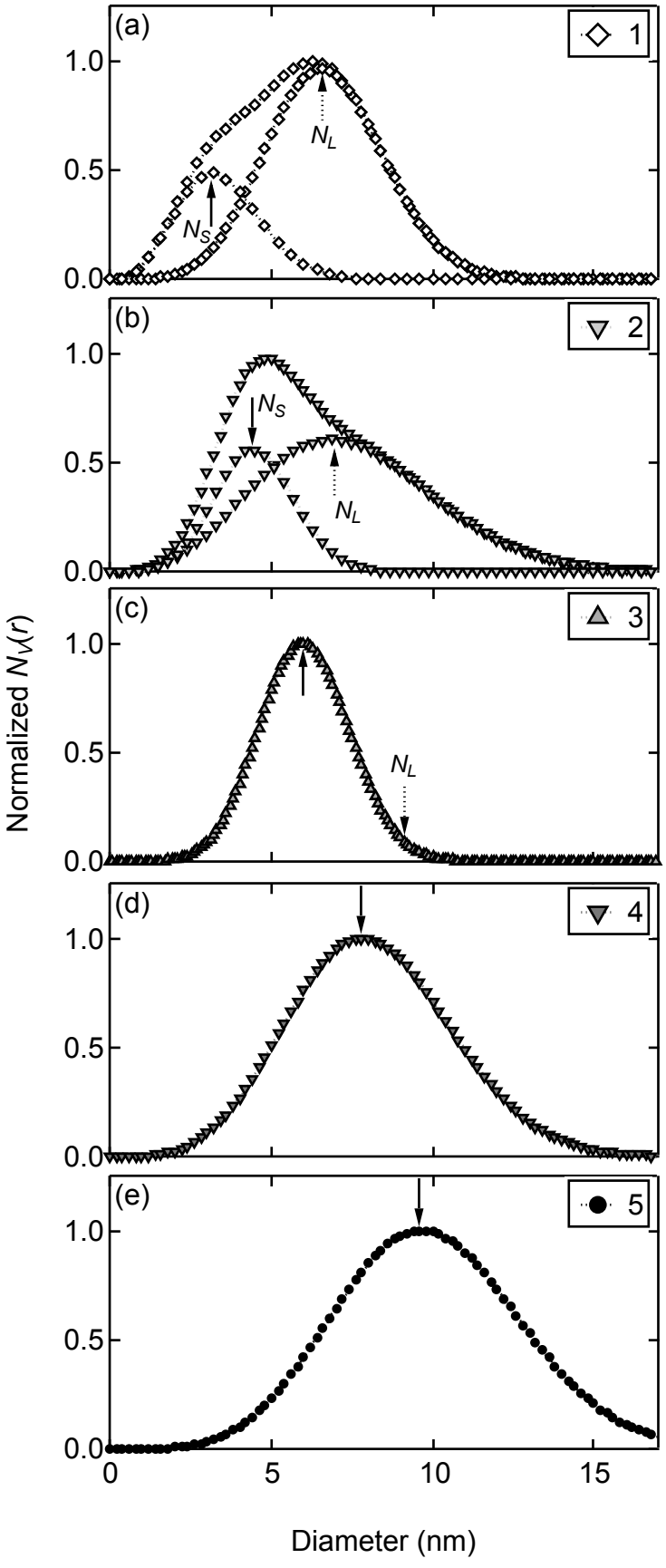
(a)
1
N_S
N_L
(b)
2
N_S
N_L
(c)
3
N_L
(d)
4
(e)
5
Normalized $N_V(r)$
Diameter (nm)
0.0
0.5
1.0
0
5
10
15

Figure 2. Volume distributions of samples (a) 1, (b) 2, (c) 3, (d) 4, and (e) 5 normalized by the peak height. With samples 1 and 2, the contributions of $N_S(r)$ and $N_L(r)$ are also shown. Solid and dotted arrows indicate the peak positions of $N_S(r)$ and $N_L(r)$, respectively. In sample 3, the dotted arrow indicates the expected position of $N_L(r)$ because this contribution probably disappears in sample 3.

Figure 2 shows $N_V(r)$ of each sample normalized by their peak heights. The contributions of both $N_S(r)$ and $N_L(r)$ are also shown (indicated by solid and dotted arrows, respectively). As compared with the contribution of $N_L(r)$ to $N_{total}(r)$ in sample 1, that in sample 2 shifts to a larger diameter and the fraction of $N_L(r)$ to $N_{total}(r)$ decreases, as indicated by the dotted arrows in figures. 2-(a) and (b). From these results, the contribution of $N_L(r)$ in sample 3 is expected to become negligible in $N_{total}(r)$, whereas the average size of $N_L(r)$ possibly increases [dotted arrow in figure 2-(c)]. In samples 4 and 5, the contribution of $N_L(r)$ also probably disappears. Based on this concept, the contribution of just $N_S(r)$ is compared (solid arrows in figures 2-(a)–(e)), where $N_S(r)$ is assumed to be identical to $N_{total}(r)$ in samples 3, 4, and 5. The peak diameter indicated by the solid arrows monotonically increases with increasing T_{sub}.

For a quantitative discussion, the volume-weighted average diameter of the nanoparticles, D_V, is shown in figure 3. The average of the total size distribution is independent of T_{sub} at low temperatures and increases with increasing T_{sub} at high temperatures. In samples 1 and 2, the average of just the contribution of $N_S(r)$ is also shown. If $N_S(r)$ in samples 3, 4, and 5 are again assumed to be identical to $N_{total}(r)$, the size of $N_S(r)$ monotonically increases from 3 to 10 nm with increasing T_{sub}. The size is sufficiently small for quantum size effects on PbSe relative to the exciton Bohr radius of 46 nm [4,5]. The increase in the size with T_{sub} also reveals that the nanoparticles grow on the substrate via thermal motion. These results ensure that the present assumption well explains the T_{sub} dependence of the size distribution. Hence, there are probably two kinds of nanoparticles with different temperature dependences in the PbSe–ZnSe composite films.

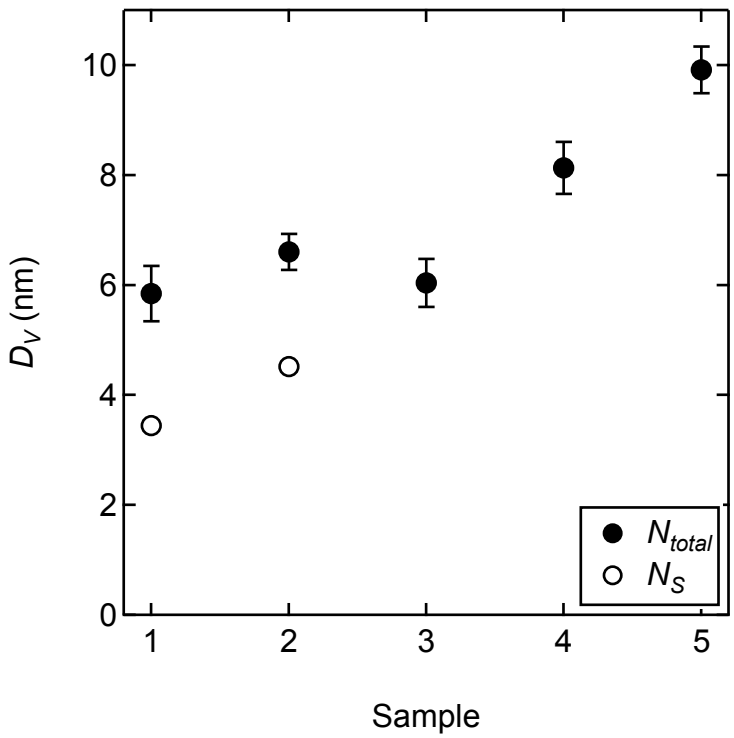

Figure 3. Substrate temperature dependence of volume-weighted average diameter. Solid and open circles are averages of total and small size distributions, respectively. In samples 3, 4, and 5, the total size distribution is equal to the small size distribution.

Next, the volume fraction and chemical composition of the nanoparticles were analyzed. The volume fraction of the nanoparticles, V_f, is expressed as $V_f = d_N V_{ave}$, where V_{ave} is an average volume. According to eq. (1) or (2), the value of $\Delta\rho$ is necessary in order to evaluate d_N from the curve fit. The parameter $\Delta\rho$ depends on the crystal structure and also on the chemical composition of the nanoparticles and the matrix. According to a previous study, the crystal structures of PbSe and ZnSe in the composite thin films are almost same as those of bulk [7]. Based on that information, the values of $\Delta\rho$ for PbSe nanoparticles in the ZnSe matrix were calculated (table 2). From these values and the results of the curve fit, V_f is evaluated (figure 4). The volume fraction of PbSe was also calculated from the chemical composition measured by EDX using the same hypothesis, that the constituent elements were completely phase-separated into PbSe and ZnSe. The volume fraction obtained in this manner is described as V_{EDX} and is

shown in figure 4. At high T_{sub} (samples 3, 4, and 5), V_f well agrees with V_{EDX}. This result clearly indicates that the PbSe nanoparticles are well separated from the ZnSe matrix at high substrate temperatures.

Table 2. $\Delta\rho$ of Pb compounds with ZnSe

Compound	$\Delta\rho$ (10^{11} cm^{-2})
PbSe	1.7
Pb	3.7
α-PbO	2.6
Pb_3O_4	2.9

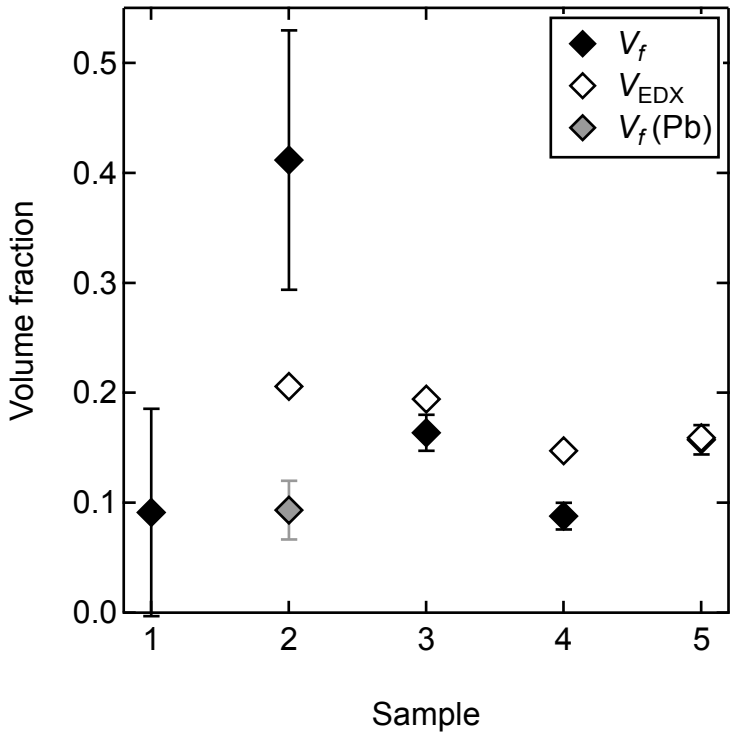

Figure 4. Substrate-temperature dependence of volume fraction of the nanoparticles. Solid and open diamonds represent V_f and V_{EDX}, respectively, evaluated under the assumption that the chemical composition is ideally separated into PbSe and ZnSe. The half-filled diamonds represent V_f, estimated under the assumption that Pb nanoparticles are formed in the ZnSe matrix.

On the other hand, V_f does not agree with V_{EDX} in sample 2. Hence, the phases in sample 2 are different from the ideal PbSe nanoparticles and the ZnSe matrix. The fact that V_f is larger than V_{EDX} shows that the present value of $\Delta\rho$ is underestimated. The possible compounds that show higher $\Delta\rho$ than PbSe against ZnSe are also listed in table 2. The calculated $\Delta\rho$ shows that pure Pb or Pb oxides can be formed instead of PbSe. Except impurities and the possibility of oxidation, Pb nanoparticles probably formed in sample 2. In this case, the Pb–Zn–Se ternary solid-solution phase is inadequate because such intermixing between the nanoparticles and the matrix reduces the difference in the electron densities and thus causes a decrease in $\Delta\rho$. In addition, the solubility limit of Zn in PbSe is quite low [7]. The q^{-4} behaviour observed in the high q region also supports the non-intermixing of PbSe and ZnSe because the index of -4 indicates that the nanoparticles have sharp interface with the matrix [19].

The validity of the formation of Pb nanoparticles is thus considered. The fragmentation of PbSe into Pb and Se during evaporation has been reported [20,21]. A similar result was also found in a study of the thermoelectric properties of PbSe thin films [22]. In this case, dissociation of PbSe was not clearly denoted, but the temperature dependence of the electromotive force in PbSe films anomalously shows a maximum between approximately 180 and 210 °C, which is between T_{sub} of samples 2 and 3. This maximum was interpreted as being due to the transition from a *p*- to an *n*-type semiconductor with increasing temperature, whereas Silverman and Levinstein claimed that the *n*-type electrical property appears due to the re-evaporation of Se from the films [20]. These studies demonstrate that the Pb nanoparticles are formed at low T_{sub}, and they suggest that Pb will be re-evaporated from the substrate or re-associated to PbSe at high T_{sub}. The value V_f of sample 2 calculated with the $\Delta\rho$ of metallic Pb is also shown in figure 4 as a half-filled plot. Since the obtained value of V_f is much lower than that of V_{EDX}, the possible nanoparticles in sample 2 are not only Pb but also PbSe. Pb is normally not a semiconductor and thus must affect the photovoltaic properties.

The above analysis of V_f and the chemical composition indicates that the PbSe nanoparticles are successfully formed at high T_{sub}, whereas the Pb nanoparticles are also generated at low T_{sub}. On the other

hand, the analysis of the size results in the formation of large nanoparticle only at low T_{sub}. From the comparison of both analyses, $N_L(r)$ and $N_S(r)$ probably correspond to the Pb and PbSe nanoparticles, respectively.

For confirmation of the SAXS analysis, x-ray diffraction (XRD) with Cu Kα radiation was performed (figure 5). The XRD patterns show the small Bragg peaks of PbSe as well as large ones of ZnSe. No clear peak of crystalline Pb was observed in samples 1 and 2. This is probably caused by its small volume fraction. The Bragg peaks of PbSe are significantly broadened and become weak with decreasing T_{sub}. The crystallite size of the PbSe $D_{Scherrer}$ was evaluated from the peak width using Scherrer's equation and is listed in Table 1 [7,23]. For sample 1, the peak intensity is too weak to properly evaluate the crystallite size. The value of $D_{Scherrer}$ increases with increasing T_{sub}. This tendency of $D_{Scherrer}$ is consistent with that of D_V estimated from SAXS. This supports the SAXS analysis. Because of the large error in $D_{Scherrer}$ due to weak intensity and high signal to background ratio, the magnitude of $D_{Scherrer}$ is not quantitatively discussed in the present study.

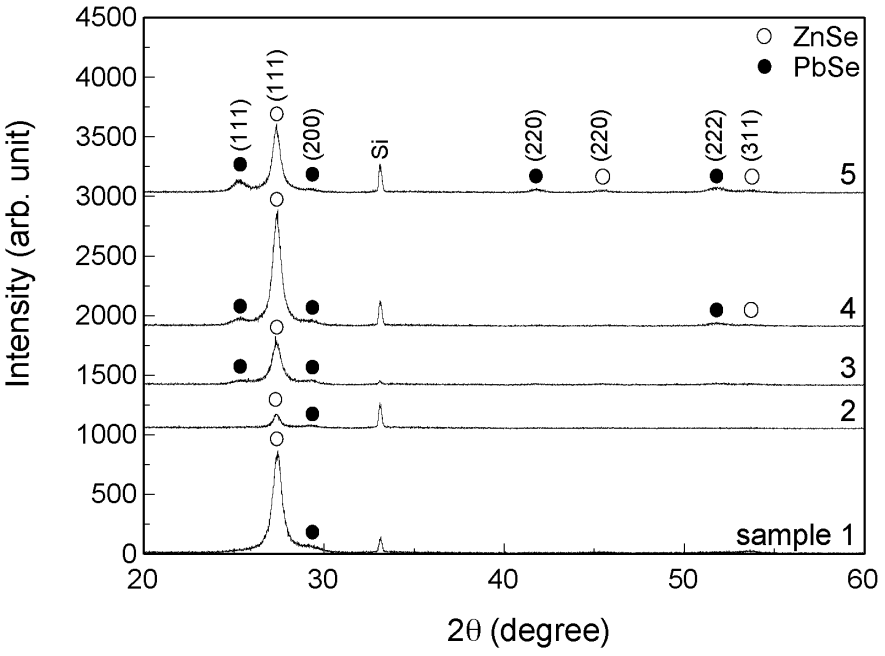

Figure 5. XRD patterns of the PbSe-ZnSe composite thin films. White and Black circles indicate the peak positions of ZnSe and PbSe. A peak of Si substrate is also obseraved.

4. Conclusion

SAXS measurements of PbSe–ZnSe composite thin films were performed. The SAXS profile changed with increasing T_{sub}. The change in the size distribution obtained from SAXS indicates the existence of two kinds of nanoparticles. From the analysis of the volume fraction and chemical composition, the nanoparticles were found to be composed of PbSe and Pb at $T_{sub} < 210$ °C. The present result shows that the obvious phase separation of PbSe–ZnSe can be obtained at $T_{sub} \geq 210$ °C. At this temperature range, the size of the PbSe nanoparticles can be controlled simply with T_{sub}. This is useful for fabricating composite thin films optimized for the solar spectrum.

Acknowledgments

This work was supported by JSPS KAKENHI Grant Numbers 24360295 and 22604003.

References

[1] Nozik A J 2002 *Physica E* **14** 115.

[2] Grätzel M 2005 *Inorg. Chem.* **44** 6841.

[3] Semonin O E, Luther J M, Choi S, Chen H-Y, Gao J, Nozik A J and Beard M C 2011 *Science* **334** 1530.

[4] Wise F W 2000 *Acc. Chem. Res.* **33** 773.

[5] Trinh M T, Houtepen A J, Schins J M, Hanrath T, Piris J, Knulst W, Goossens A P L M and Siebbeles L D A 2008 *Nano Lett.* **8** 1713.

[6] Yun D, Feng W, Wu H and Yoshino K 2009 *Sol. Energy Mater. Sol. Cells* **93** 1208.

[7] Abe S 2011 *Nanoscale Res. Lett* **6** 324.

[8] Arivazhagan V, Parvathi M M, Rajesh S, Sæterli R and Holmestad R 2013 *Appl. Phys. Lett.* **102** 242110.

[9] Hono K and Ohnuma M 2002 *Magnetic Nanostructures* ed Nalwa H S (California: American Scientific Publishers) pp 327–358.

[10] Pauw B R 2013 *J. Phys. Condens. Matter* **25** 383201.

[11] Kagan C R, Murray C B and Bawendi M G 1996 *Phys. Rev. B* **54** 8633.

[12] Abe S, Ohnuma M, Ping D H and Ohnuma S 2008 *J. Appl. Phys.* **104** 104305.

[13] Oba Y, Ohnuma M, Ohnuma S, Furusaka M, Koppoju S and Takeda S 2013 *J. Magn. Magn. Mater.* **334** 45.

[14] Zhang F, Ilavsky J, Long G G, Quintana J P G, Allen A J and Jemian P R 2010 *Metall. Mater. Trans. A* **41** 1151.

[15] Pedersen J S 1997 *Adv. Colloid Interface Sci.* **70** 171.

[16] Pedersen J S 1994 *J. Appl. Cryst.* **27** 595.

[17] Jemian P R and Allen A J 1994 *J. Appl. Cryst.* **27** 693.

[18] Ilavsky J and Jemian P R 2009 *J. Appl. Cryst.* **42** 347.

[19] Koberstein J T, Morra B and Stein R S 1980 *J. Appl. Cryst.* **13** 34.

[20] Silverman S J and Levinstein H 1954 *Phys. Rev.* **94** 871

[21] Porter R F 1961 *J. Chem. Phys.* **34** 583.

[22] Das V D and Bhat K S 1990 *J. Mater. Sci. – Mater. Electron.* **1** 169.

[23] Guinier A 1994 *X-Ray Diffraction In Crystals, Imperfect Crystals, and Amorphous Bodies* (New York: Dover Publications).